JOURNAL OF AIRCRAFT
Vol. 47, No. 4, July–August 2010

Reynolds-Stress Model Flow Prediction in Aircraft-Engine Intake Double-S-Shaped Duct

G. A. Gerolymos*
Université Pierre-et-Marie-Curie, 75005 Paris, France
S. Joly† and M. Mallet‡
Dassault-Aviation, 92552 St. Cloud, France
and
I. Vallet§
Université Pierre-et-Marie-Curie, 75005 Paris, France

DOI: 10.2514/1.47538

The purpose of the present paper is to assess the predictive capability of Reynolds-averaged Navier–Stokes computations using seven-equation Reynolds-stress model wall-normal-free closures for flows in aircraft-engine intake double-S-duct configurations. The intake studied operates at high subsonic Mach numbers and is characterized by high turning angle of the second S-leg, inducing a particularly complex flow structure up to the engine face. Computations were run using two wall-topology-free second-moment closures and a baseline two-equation model, carefully checked for grid convergence, and compared with available experimental measurements. Computational data were then used to analyze the flowfield structure.

I. Introduction

MANY aircraft-engine installations include complex-shaped intake ducts, through which the airflow enters the engine: e.g., center engines [1], combat [2] and/or supersonic [3] aircraft, unmanned air vehicles [4], and unmanned combat air vehicles [5]. Space limitations [6] and/or stealth [7,8] requirements may lead to particularly flow-unfriendly shapes [9]. The accurate prediction of the flow through such diffusing transition ducts is essential for the design and evaluation of aircraft propulsion systems [10,11]. The total-pressure distortion at the engine face [12], induced by the particular form of the duct, has a major impact on engine performance, as this distortion propagates inside the engine [13], dramatically modifying the compression system stability limits [14]. The precise impact of the intake depends on the inhomogeneity it induces at the engine face, also called the aerodynamic-interface plane (AIP [6,8,9]). The effect of inhomogeneity is much more important than the average value of loss [12–14], requiring accurate prediction of the flow structure. This flow distortion is the result of various physical mechanisms, associated with the complex geometry of aircraft-engine diffusing ducts [10,11] (combining, for example, substantial cross-sectional form change [9] with S-shaped centerline [15] and area-change-induced diffusion effect [16], even including offplane centerline shapes [17]). This puts stringent requirements on the performance of the turbulence model, because of the associated complex 3-D flows [18] (complex strains, massive flow separation, secondary flows, relaxation and mixing).

The throughflow projection of the centerline of S-shaped ducts consists of 1 S-like bend, between two straight parts. If the length of the duct is short and/or the adverse pressure gradient induced by area increase is high, severe separation appears in the initial part of the S [15,16], the flow subsequently relaxing in the aft part. In this respect, the S-duct is characterized by the evolution of its centerline (S-shape) and of its cross section (form and/or area).

The term *double-S-shaped ducts* was coined by Tormalm [6], but such ducts had also been studied by Rabe [19], Brear et al. [9], and Kirk et al. [8], although these authors [8,9,19] loosely called them serpentine ducts. Tormalm [6] states that,

> When considering the complete propulsion system, the inlet design is always depending on the exit nozzle length,. . .a longer nozzle. . ., which is essential in reducing the signature, requir[ing] a short inlet; . . . double-S-bend designs were created to solve [the] problem [of space], thus raising the engine into a more central position.

Double-S-shaped ducts (2S-ducts) are formed by joining together two S-ducts: a descending one followed by an ascending one (or vice versa). In such ducts, the flow, after undergoing separation in the first S-leg, is further subjected to adverse pressure-gradient in the second S-leg, before relaxing in the aft straight part. The flow at the entrance of the second S-leg is highly perturbed (indeed separated) so that methods predicting tolerably well the flow in an S-duct may fail in predicting the flow in a 2S-duct.

Several previous comparisons of numerical computations with measurements in S-ducts [15,20–27] and in 2S-ducts [6,8,9] highlight the increasing difficulty of correctly predicting such flows, as the centerline-turning and the area-ratio-induced diffusion increase. A rather comprehensive review of published comparisons between computations and measurements in S-ducts was given by Kirk et al. [8]. It is not a simple task to draw a general conclusion from these comparisons, not only because of differences in grid resolution (coarse-grid calculations in the 1990s [15,20–22] compared to quasi-grid-converged computations in more recent work [6,8,23,27]), but also because of differences in the computational domain (location of inflow/outflow boundaries) and of differences in the numerical method (Kirk et al. [8] obtained substantial differences in the results at the AIP using the same turbulence model but different numerical methods and grids). Furthermore, it is of fundamental importance to consider, when evaluating turbulence model performance, comparison with all available experimental data, since in some instances seemingly satisfactory distributions of wall pressures correspond to very unsatisfactory total-pressure distribution at the AIP. In general, [8,9,15,20–24,26], despite the scatter in computed data and the sometimes partial comparison with measurements, and despite the absence of systematic evaluation of all types of models using the same numerical method (indeed code) and grid, it appears that

Presented as Paper 2009-4161 at the 39th AIAA Fluid Dynamics Conference, San Antonio, TX, 22–25 June 2009; received 9 October 2009; accepted for publication 24 February 2010.

*Case 161, 4 Place Jussieu; georges.gerolymos@upmc.fr.
†78 Quai Marcel Dassault; sylvain.joly@dassault-aviation.com.
‡78 Quai Marcel Dassault; michel.mallet@dassault-aviation.com.
§Case 161, 4 Place Jussieu; isabelle.vallet@upmc.fr.

two-equation models perform better than zero-equation or one-equation models [8].

Many authors have stressed the fundamental importance of using "anisotropy-resolving closures" (a term coined by Leschziner [28]) in turbulence modeling, not only for Reynolds-averaged Navier–Stokes, but also for subgrid-modeling in large-eddy simulation applications [29] and this seems particularly relevant for the complex flows in S-ducts [27] and 2S-ducts. Most of the published computational studies [8,9,15,20–24,26] of S-duct or 2S-duct flows use the Boussinesq hypothesis [18], with the exception of Tormalm [6], who used an explicit algebraic Reynolds-stress model [18] and Vallet [27], who used differential Reynolds-stress models [18,30–32] (RSMs).

The purpose of the present paper is to evaluate different turbulence models on a more realistic aircraft intake 2S-duct geometry, tested experimentally at ONERA.¶ Contrary to previous investigations [6,8,9], the turning angle of the second S-leg is of the same order of magnitude as that of the first S-leg, so that the engine face, also called the aerodynamic-interface plane (AIP [6,8,9]), is located at approximately the same height as the inlet of the intake, thus optimizing available space. On the other hand, the resulting flow is substantially more complicated than in previous designs [6,8,9], where the second S-leg turning angle was small. Computations using two wall-normal-free (WNF [32]) RSMs are compared with available measurements and with the baseline Launder–Sharma (LS) [33] k-ε model to assess their performance in this difficult flow. Among the differences between the two RSMs, that with the greatest influence on the results is the functional dependence on the Reynolds-stress-tensor anisotropy flatness parameter [34] A of the coefficient used in the isotropization of production (IP [18,35]) model of the homogeneous part of the rapid-redistribution terms [32]. In the Gerolymos–Vallet (GV) [31] RSM, the IP coefficient C_ϕ^{RH} is close to the usual values [35] in the logarithmic wall layer ($A \in [0, .55]$), but is sharply raised as A approaches unity, to correctly model flows with large separation and other complex strains [27,36]. The WNF–LSS [32] RSM is a wall-topology-free extension of the Launder–Shima–Sharma (LSS) [30,35] RSM and, like the wall-topology-dependent [30,35] RSM, performs less well than the GV RSM in the presence of large separation [27,36].

II. RSM System of Equations

A. Mean Flow Equations

The flow is modeled by the compressible Favre–Reynolds-averaged 3-D Navier–Stokes equations [30,31]:

$$\frac{\partial \bar\rho}{\partial t} + \frac{\partial \bar\rho \tilde u_\ell}{\partial x_\ell} = 0 \tag{1a}$$

$$\frac{\partial \bar\rho \tilde u_i}{\partial t} + \frac{\partial}{\partial x_\ell}[\bar\rho \tilde u_i \tilde u_\ell + \bar p \delta_{i\ell}] - \frac{\partial}{\partial x_\ell}[\bar\tau_{i\ell} - \overline{\rho u_i'' u_\ell''}] = 0 \tag{1b}$$

$$\begin{aligned}\frac{\partial}{\partial t}[\bar\rho \check h_t - \bar p] + \frac{\partial \bar\rho \tilde u_\ell \check h_t}{\partial x_\ell} - \frac{\partial}{\partial x_\ell}[\tilde u_i(\bar\tau_{i\ell} - \overline{\rho u_i'' u_\ell''}) \\ - (\bar q_\ell + \overline{\rho h'' u_\ell''})] = S_{\check h_t}\end{aligned} \tag{1c}$$

where t is the time, x_ℓ are the Cartesian space coordinates, u_i are the velocity components, ρ is the density, p is the pressure, δ_{ij} is the Kronecker symbol, tildes denote Favre averaging, overbars denote nonweighted averaging, double primes are Favre fluctuations, primes are nonweighted fluctuations, $\check h_t = \tilde h + \frac{1}{2}\tilde u_i \tilde u_i$ is the total enthalpy of the mean flow, h is the specific enthalpy, $-\overline{\rho u_i'' u_j''} = -\bar\rho \widetilde{u_i'' u_j''}$ are the Reynolds stresses, $k = \frac{1}{2}\widetilde{u_i'' u_i''}$ is the turbulence kinetic energy (TKE), τ_{ij} are the viscous stresses, q_ℓ is the molecular heat flux, $\overline{\rho h'' u_\ell''} = \bar\rho \widetilde{h'' u_\ell''}$ is the turbulent heat flux, and $S_{\check h_t}$ is a source term appearing in the mean flow energy equation [30,31]. The symbol $\check{}$ is used to denote a function of average quantities that is neither a Favre average nor a nonweighted average.

¶Private communication with A. L. Vuillerme, ONERA, Châtillon, France, December 2006.

The source term appearing in the mean flow energy equation is obtained by combining the averaged energy equation with the transport equation for the turbulence kinetic energy and reads [30]

$$S_{\check h_t} = \left[\Pi_k - P_k + \bar\rho \varepsilon_k^{(\tau)} + \overline{u_i''}\frac{\partial \bar p}{\partial x_i} + \bar\tau_{i\ell}\frac{\partial \overline{u_i''}}{\partial x_\ell}\right] \tag{2}$$

where $\Pi_k = \frac{1}{2}\Pi_{\ell\ell}$ is the velocity-pressure-gradient correlation in the TKE transport equation ($\Pi_{ij} = \overline{u_i' \partial_{x_j} p' + u_j' \partial_{x_i} p'}$), $P_k = \frac{1}{2}P_{\ell\ell}$ is the TKE production, and $\varepsilon_k^{(\tau)} = \frac{1}{2}\varepsilon_{\ell\ell}^{(\tau)}$ is the TKE dissipation rate.

B. Reynolds-Stress Transport

The transport equations for the Favre–Reynolds-averaged Reynolds stresses are [31]

$$\begin{aligned}&\underbrace{\frac{\partial \overline{\rho u_i'' u_j''}}{\partial t} + \frac{\partial}{\partial x_\ell}(\overline{\rho u_i'' u_j''} \tilde u_\ell)}_{\text{convection } C_{ij}} \\ &= \underbrace{\frac{\partial}{\partial x_\ell}(-\overline{\rho u_i'' u_j'' u_\ell''} - \overline{p' u_j'}\delta_{i\ell} - \overline{p' u_i'}\delta_{j\ell} + \overline{u_i' \tau_{j\ell}'} + \overline{u_j' \tau_{i\ell}'})}_{\text{diffusion } d_{ij} = d_{ij}^{(u)} + d_{ij}^{(p)} + d_{ij}^{(\tau)}} \\ &+ \underbrace{\overline{p'\left(\frac{\partial u_i'}{\partial x_j} + \frac{\partial u_j'}{\partial x_i} - \frac{2}{3}\frac{\partial u_k'}{\partial x_k}\delta_{ij}\right)}}_{\text{redistribution } \phi_{ij}} \\ &+ \underbrace{\left(-\overline{\rho u_i'' u_\ell''}\frac{\partial \tilde u_j}{\partial x_\ell} - \overline{\rho u_j'' u_\ell''}\frac{\partial \tilde u_i}{\partial x_\ell}\right)}_{\text{production } P_{ij}} + \underbrace{\frac{2}{3}\overline{p'\frac{\partial u_k'}{\partial x_k}}\delta_{ij}}_{\text{pressure-dilatation } \frac{2}{3}\phi_p \delta_{ij}} \\ &+ \underbrace{\left(-\overline{u_i''}\frac{\partial \bar p}{\partial x_j} - \overline{u_j''}\frac{\partial \bar p}{\partial x_i} + \overline{u_i''}\frac{\partial \bar\tau_{j\ell}}{\partial x_\ell} + \overline{u_j''}\frac{\partial \bar\tau_{i\ell}}{\partial x_\ell}\right)}_{\text{density fluctuation effects } K_{ij}} \\ &- \underbrace{\left(\overline{\tau_{j\ell}'\frac{\partial u_i'}{\partial x_\ell} + \tau_{i\ell}'\frac{\partial u_j'}{\partial x_\ell}}\right)}_{\text{dissipation } \bar\rho \varepsilon_{ij}^{(\tau)}}\end{aligned} \tag{3}$$

Introducing an exact term for the viscous diffusion of the Reynolds stresses ($d_{ij}^{(\mu)}$) instead of the original term ($d_{ij}^{(\tau)}$), this exact equation is recast in the following mathematically equivalent form, which is actually modeled

$$\begin{aligned}&\underbrace{\frac{\partial \overline{\rho u_i'' u_j''}}{\partial t} + \frac{\partial}{\partial x_\ell}(\overline{\rho u_i'' u_j''} \tilde u_\ell)}_{\text{convection } C_{ij}} \\ &= \underbrace{\frac{\partial}{\partial x_\ell}\left(-\overline{\rho u_i'' u_j'' u_\ell''} - \overline{p' u_j'}\delta_{i\ell} - \overline{p' u_i'}\delta_{j\ell} + \mu\overline{\frac{\partial u_i' u_j'}{\partial x_\ell}}\right)}_{\text{diffusion } d_{ij} = d_{ij}^{(u)} + d_{ij}^{(p)} + d_{ij}^{(\mu)}} \\ &+ \underbrace{\overline{p'\left(\frac{\partial u_i'}{\partial x_j} + \frac{\partial u_j'}{\partial x_i} - \frac{2}{3}\frac{\partial u_k'}{\partial x_k}\delta_{ij}\right)}}_{\text{redistribution } \phi_{ij}} \\ &+ \underbrace{\left(-\overline{\rho u_i'' u_\ell''}\frac{\partial \tilde u_j}{\partial x_\ell} - \overline{\rho u_j'' u_\ell''}\frac{\partial \tilde u_i}{\partial x_\ell}\right)}_{\text{production } P_{ij}} + \underbrace{\frac{2}{3}\overline{p'\frac{\partial u_k'}{\partial x_k}}\delta_{ij}}_{\text{pressure-dilatation } \frac{2}{3}\phi_p \delta_{ij}} \\ &+ \underbrace{\left(-\overline{u_i''}\frac{\partial \bar p}{\partial x_j} - \overline{u_j''}\frac{\partial \bar p}{\partial x_i} + \overline{u_i''}\frac{\partial \bar\tau_{j\ell}}{\partial x_\ell} + \overline{u_j''}\frac{\partial \bar\tau_{i\ell}}{\partial x_\ell}\right)}_{\text{density fluctuation effects } K_{ij}} \\ &- \underbrace{\left(\frac{\partial}{\partial x_\ell}\left[\mu\overline{\frac{\partial u_i' u_j'}{\partial x_\ell}}\right] - \left(\overline{u_i'\frac{\partial \tau_{j\ell}'}{\partial x_\ell} + u_j'\frac{\partial \tau_{i\ell}'}{\partial x_\ell}}\right)\right)}_{\text{dissipation } \bar\rho \varepsilon_{ij}^{(\mu)}}\end{aligned} \tag{4}$$

where μ is the dynamic viscosity. Convection C_{ij}, production P_{ij}, and viscous diffusion $d_{ij}^{(\mu)}$ are exact terms, whereas all the other terms ($d_{ij}^{(u)}$, $d_{ij}^{(p)}$, ϕ_{ij}, ϕ_p, K_{ij}, and $\varepsilon_{ij}^{(\mu)}$) require modeling. Two different near-wall low-Reynolds-number Reynolds-stress models (RSMs) developed by the authors [31,32] were used in the present work. Both models [31,32] are completely WNF: i.e., completely independent of wall topology (distance-from-the-wall vector) [32]. The details on the development of the models [31,32] are beyond the scope of the present paper. The general tensorial form of the modeled terms and the corresponding model-coefficient functions are briefly described in the following WNF–IPRI RSMs subsection (Sec. II.C).

C. Wall-Normal-Free Isotropization-of-Production/ Return-to-Isotropy Reynolds-Stress Models

The Reynolds-stress transport Eqs. (4) are written as

$$C_{ij} = \frac{\partial}{\partial x_\ell}(\mathcal{D}_{ij\ell}^{(u)} + \mathcal{D}_{ij\ell}^{(p)} + \mathcal{D}_{ij\ell}^{(\mu)}) + P_{ij} - \frac{2}{3}\bar{\rho}\varepsilon\delta_{ij} + \left[\phi_{ij}^S - (\bar{\rho}\varepsilon_{ij}^{(\mu)} - \frac{2}{3}\bar{\rho}\varepsilon\delta_{ij})\right] + \phi_{ij}^R + K_{ij} + \frac{2}{3}\phi_p\delta_{ij} \tag{5}$$

where $\phi_{ij} = \phi_{ij}^S + \phi_{ij}^R$. The Reynolds-stress closures used [31,32] (which neglect the strong compressibility effects K_{ij} and ϕ_p and the pressure-velocity correlations $\mathcal{D}_{ij\ell}^{(p)}$) can be written in the general form:

$$K_{ij} = 0 \qquad \phi_p = 0 \qquad \mathcal{D}_{ij\ell}^{(p)} = 0$$

$$\left[\phi_{ij}^S - \left(\bar{\rho}\varepsilon_{ij} - \frac{2}{3}\bar{\rho}\varepsilon\delta_{ij}\right)\right] = -C_\phi^{SH}\bar{\rho}\varepsilon a_{ij} + C_\phi^{SI}\frac{\varepsilon}{k}\left(\overline{\rho u_n'' u_m''}e_n^I e_m^I\delta_{ij} - \frac{3}{2}\overline{\rho u_n'' u_i''}e_n^I e_j^I - \frac{3}{2}\overline{\rho u_n'' u_j''}e_n^I e_i^I\right)$$

$$\phi_{ij}^{RH} = -C_\phi^{RH}\left(P_{ij} - \frac{1}{3}P_{mm}\delta_{ij}\right)$$

$$\phi_{ij}^R = \phi_{ij}^{RH} + C_\phi^{RI}\left(\phi_{mm}^{RH}e_n^I e_m^I\delta_{ij} - \frac{3}{2}\phi_{in}^{RH}e_n^I e_j^I - \frac{3}{2}\phi_{jn}^{RH}e_n^I e_i^I\right)$$

$$\mathcal{D}_{ij\ell}^{(u)} = C_u^S\frac{k}{\varepsilon}\left(\bar{\rho}\,\widetilde{u_\ell'' u_k''}\frac{\partial\widetilde{u_i'' u_j''}}{\partial x_k}\right) + C_{u_1}^S\frac{k}{\varepsilon}\bar{\rho}G_{ij\ell}^S$$

$$\mathcal{D}_{ij\ell}^{(\mu)} = \breve{\mu}\frac{\partial\widetilde{u_i'' u_j''}}{\partial x_k}\delta_{k\ell} \tag{6}$$

with

$$G_{ij\ell}^S = \widetilde{u_i'' u_k''}\frac{\partial\widetilde{u_j'' u_\ell''}}{\partial x_k} + \widetilde{u_j'' u_k''}\frac{\partial\widetilde{u_i'' u_\ell''}}{\partial x_k} + \widetilde{u_\ell'' u_k''}\frac{\partial\widetilde{u_i'' u_j''}}{\partial x_k} \qquad \varepsilon = \frac{1}{2}\varepsilon_{\ell\ell}^{(\mu)} \tag{7}$$

where the superscripts R and S denote the rapid and the slow parts [18,32,34,35] of the pressure-strain correlation ϕ_{ij}, the superscripts H and I denote the homogeneous and inhomogeneous parts of the pressure-strain correlation ϕ_{ij}, and ε is the TKE dissipation rate determined from the modified dissipation-rate transport equation ε^* (Sec. II.D).

These Reynolds-stress models are wall-normal-free (independent of any wall-topology parameter) by using the unit vector $\mathbf{e}^I = \mathbf{e}^I(\ell_T, A_2, A, Re_T)$, pointing in the inhomogeneity direction, developed by Gerolymos and Vallet [31] and Gerolymos et al. [32]:

$$\mathbf{e}^I = e_\ell^I\mathbf{e}_\ell^I = \frac{\operatorname{grad}\left(\frac{\ell_T[1-e^{-\frac{Re_T^*}{30}}]}{1+2\sqrt{A_2+2A^{16}}}\right)}{\left\|\operatorname{grad}\left(\frac{\ell_T[1-e^{-\frac{Re_T^*}{30}}]}{1+2\sqrt{A_2+2A^{16}}}\right)\right\|} \Rightarrow \|\mathbf{e}^I\| = \sqrt{e_\ell^I e_\ell^I} = 1 \tag{8}$$

where ℓ_T is the turbulent length scale, Re_T is the turbulent Reynolds number [Re_T^* is the turbulent Reynolds number based on the modified dissipation rate (cf. Sec. II.D)], A_2 and A_3 are the invariants of the turbulence anisotropy tensor a_{ij}, and A is the flatness parameter introduced by Lumley [34]:

$$a_{ij} = \frac{\widetilde{u_i'' u_j''}}{k} - \frac{2}{3}\delta_{ij}; \qquad A_2 = a_{ik}a_{ki};$$

$$A_3 = a_{ik}a_{kj}a_{ji}; \qquad A = \left[1 - \frac{9}{8}(A_2 - A_3)\right] \tag{9a}$$

$$\ell_T = \frac{k^{\frac{3}{2}}}{\varepsilon}; \qquad Re_T = \frac{k^2}{\breve{\nu}\varepsilon}; \qquad Re_T^* = \frac{k^2}{\breve{\nu}\varepsilon^*} \tag{9b}$$

Different values for the coefficients C_ϕ^{SH}, C_ϕ^{SI}, C_ϕ^{RH}, C_ϕ^{RI}, C_u^S, and $C_{u_1}^S$ correspond to the WNF RSMs used in the present computations (Table 1). Note that the C_ϕ^{SH} coefficient proposed by Launder and Shima [35] is common to both models contrary to the C_ϕ^{RH} coefficient that was modified by Gerolymos and Vallet [31] in the GV RSM to improve the potential of the model to predict flows with important separation. The coefficients C_ϕ^{SI} and C_ϕ^{RI}, which take into account the wall-echo effect [18,32,35] without using any geometric parameters such as distance from the solid wall, have been tuned to give similar results (for both models) for zero-pressure-gradient flat-plate boundary-layer flow [31,32].

The WNF–LSS [32] RSM is a wall-normal-free version of the Launder–Shima–Sharma [30] RSM, which uses wall normals and distances from the wall. This model was developed to highlight the importance of the rapid-redistribution term for the prediction of separated flow. Indeed, in conjunction with the use of the inhomogeneity-direction unit vector $\mathbf{e}^I$ [Eq. (8)] the coefficient function $C_\phi^{RH}(A, Re_t)$ for the rapid-redistribution term [Eq. (6); Table 1] developed by Gerolymos and Vallet [31] substantially improves the capacity of the model to predict large separation [27,32,36]. This observation is further substantiated by the results of the present study (Sec. III).

Table 1 Coefficients used in the Reynolds-stress models [Eq. (7)]

Coefficients[a]	WNF–LSS RSM [32]	GV RSM [31]
C_u^S	0.22	0.
$C_{u_1}^S$	0.	0.11
C_ϕ^{SH}		$1 + 2.58AA_2^{\frac{1}{4}}[1 - e^{-(\frac{Re_T}{150})^2}]$
C_ϕ^{RH}	$0.75\sqrt{A}$	$0.75\sqrt{A}[1 - \max(0, 1 - \frac{Re_T}{50})]$ if A < 0.55
C_ϕ^{RH}	$0.75\sqrt{A}$	$[0.75 + 1.3(A - 0.55)A^{0.5-1.3(A-0.55)}][1 - \max(0, 1 - \frac{Re_T}{50})]$ if $0.55 \le$ A $< 0.55 + \frac{0.25}{1.3}$
C_ϕ^{RH}	$0.75\sqrt{A}$	$A^{\frac{1}{4}}[1 - \max(0, 1 - \frac{Re_T}{50})]$ if $0.55 + \frac{0.25}{1.3} \le$ A ≤ 1
C_ϕ^{SI}	$0.90[1 - \frac{2}{3}(C_\phi^{SH} - 1)]\left\|\operatorname{grad}\left(\frac{\ell_T[1-e^{-\frac{Re_T^*}{30}}]}{1+1.8A_2^{0.8}}\right)\right\|$	$0.83[1 - \frac{2}{3}(C_\phi^{SH} - 1)]\left\|\operatorname{grad}\left(\frac{\ell_T[1-e^{-\frac{Re_T^*}{30}}]}{1+2A_2^{0.8}}\right)\right\|$
C_ϕ^{RI}	$\max\left[\frac{2}{3} - \frac{1}{6C_\phi^{RH}}, 0\right]\left\|\operatorname{grad}\left(\frac{\ell_T[1-e^{-\frac{Re_T^*}{30}}]}{1+1.8A_2^{\max(0.6,A)}}\right)\right\|$	

[a]Note that R is rapid [34], S is slow [34], H is homogeneous [32], and I is inhomogeneous [32].

D. Scale-Determining Equation and Other Terms

The Reynolds-stress-transport (RST) equations. (5) are completed by an equation for the modified [33] dissipation rate $\varepsilon^* = \varepsilon - 2\breve{\nu}[\mathrm{grad}(\sqrt{k})]^2$. The modeled form of the ε^* equation is [30]

$$\frac{\partial \bar{\rho}\varepsilon^*}{\partial t} + \frac{\partial}{\partial x_\ell}(\bar{\rho}\varepsilon^* \tilde{u}_\ell) = \underbrace{\frac{\partial}{\partial x_\ell}\left[\left(C_\varepsilon \frac{k}{\varepsilon^*}\overline{\rho u_k'' u_\ell''} + \breve{\mu}\delta_{k\ell}\right)\frac{\partial \varepsilon^*}{\partial x_k}\right]}_{\frac{\partial \mathcal{D}_{\varepsilon_\ell}}{\partial x_\ell}}$$
$$+ \underbrace{C_{\varepsilon 1} P_k \frac{\varepsilon^*}{k} - C_{\varepsilon 2}\bar{\rho}\frac{\varepsilon^{*2}}{k} + 2\breve{\mu}C_\mu \frac{k^2}{\varepsilon^*}\left(\frac{\partial^2 \tilde{u}_i}{\partial x_\ell \partial x_\ell}\frac{\partial^2 \tilde{u}_i}{\partial x_m \partial x_m}\right)}_{S_\varepsilon} \quad (10)$$

The Launder–Sharma ε-equation coefficients [33] are

$$C_\mu = 0.09 e^{-\frac{3.4}{(1+0.02Re_T^*)^2}}; \qquad C_\varepsilon = 0.18;$$
$$C_{\varepsilon 1} = 1.44; \qquad C_{\varepsilon 2} = 1.92(1 - 0.3e^{-Re_T^{*2}}) \quad (11)$$

Standard approximations [31] are used for the turbulent heat flux $\overline{\rho u_i'' h''}$, and for $\bar{\tau}_{ij}$ and $\bar{q}_i$,

$$\overline{\rho u_i'' h''} = -\frac{\mu_T c_p}{Pr_T}\frac{\partial \tilde{T}}{\partial x_i}; \qquad Pr_T = 0.9;$$
$$\mu_T = C_\mu \breve{\mu} Re_T^*; \qquad \bar{\tau}_{ij} = 2\breve{\mu}\left(\breve{S}_{ij} - \frac{1}{3}\breve{S}_{\ell\ell}\delta_{ij}\right);$$
$$\breve{S}_{ij} = \frac{1}{2}\left(\frac{\partial \tilde{u}_i}{\partial x_j} + \frac{\partial \tilde{u}_j}{\partial x_i}\right); \qquad \bar{q}_i = -\breve{\lambda}\frac{\partial \tilde{T}}{\partial x_i} \quad (12)$$

where λ is the heat conductivity, μ_T is eddy viscosity and $\breve{S}_{ij}$ is the mean flow rate-of-strain tensor. Finally, the source term in the energy Eq. (2) is modeled by [30,31]

$$S_{\breve{h}_t} = -P_k + \bar{\rho}\varepsilon \quad (13)$$

The values of thermodynamic constants (including molecular viscosity and heat conductivity) correspond to air as working medium [31].

E. Numerical Method

The numerical calculations were performed using a multiblock implicit upwind-biased multigrid solver [37,38]. The five mean flow (MF) and the seven RST equations were discretized on multiblock structured grids [37] via MUSCL3 upwind-biased reconstruction [37,38] of the primitive variables, used to construct the numerical fluxes based on the HLLCh (hybrid Harten–Lax–van Leer–contact) approximate Riemann solver [38]. It is important to note that the same $O(\Delta x^3)$ (for smooth flows on homogeneous grids) reconstruction is used both for the mean flow and for the turbulence variables. This in no way degrades the numerical stability of the method. What is important for stability is the compatibility of the approximate Riemann solver with the coupled MF/RST set of equations, or the use of a hybrid approximate Riemann solver [38].

Time integration uses a dual-time-stepping approach with implicit subiterations [37,38], and convergence is accelerated using mean flow multigrid [37,38]. Explicit realizability constraints are applied [30] at various steps of the algorithm [37]. In the computations presented in the present paper, we used a $[\mathrm{CFL}, \mathrm{CFL}^*; M_{\mathrm{it}}, r_{\mathrm{TRG}}] = [100, 10; -, -1]$ subiterative strategy [37,38] [CFL (Courant–Friedrichs–Lewy) defines the physical time step [37], CFL^* defines the dual time step [37], and r_{TRG} is the subiterative convergence tolerance, which dynamically adjusts the number of subiterations M_{it} at every iteration), with three levels of sawtooth $V(1,0)$ multigrid [37,38].

III. Results

A. Configuration

The configuration studied in the present work is a diffusing 2S-duct of elliptic cross section at the inlet and of circular cross section at the outlet (Fig. 1). This test case, studied experimentally at ONERA (see footnote ¶), corresponds to high-subsonic-Mach- number

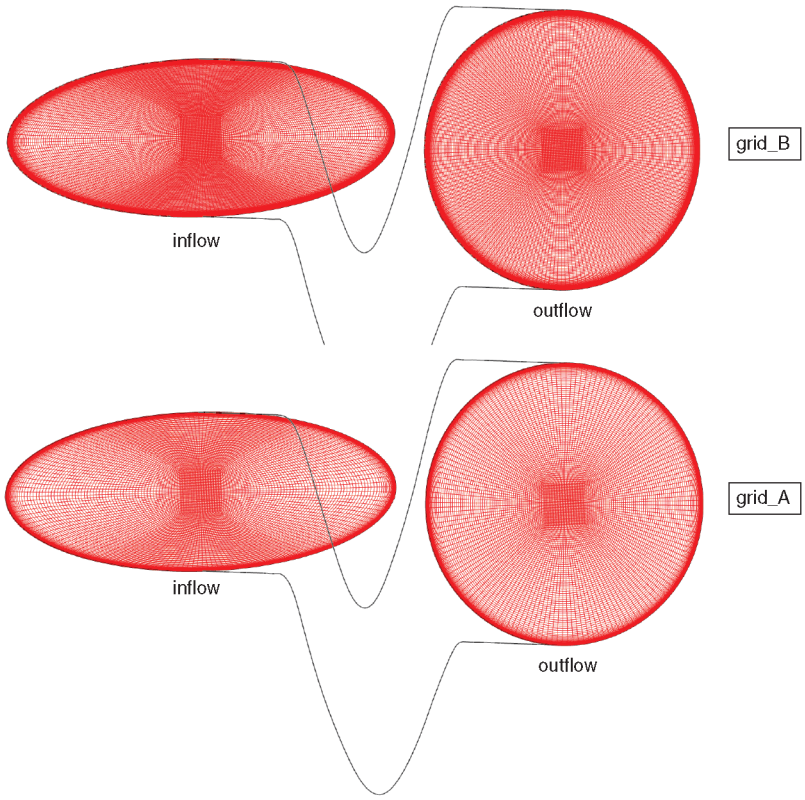

Fig. 1 View of the computational grids at the inlet and the outlet of the computational domain of the double-S-shaped duct (2.9×10^6 points for grid_A and 6.2×10^6 points for grid_B).

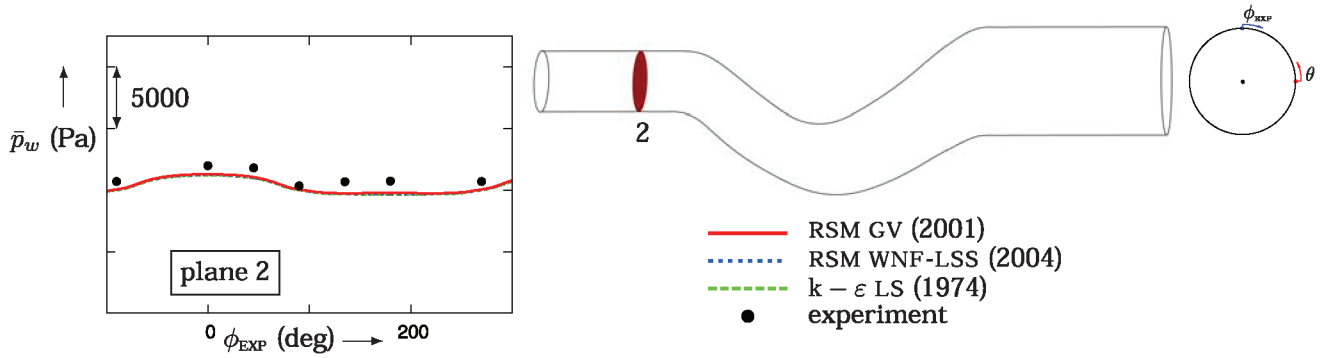

Fig. 2 Comparison of experimental wall-static-pressure $\bar{p}_w$ distributions in the circumferential direction ϕ_{EXP} at the inflow of the experimental domain (plane 2) with computations using the GV [31] and the WNF–LSS [32] RSMs and the LS k-ε model [33] (2.9×10^6 points for grid_A).

operation and presents a large recirculation zone on the duct floor. Available measurements include wall-static-pressure taps and rake measurements of total and static pressure (from which the Mach number is estimated) at the engine face (AIP). The complex form and high diffusion of the duct induce massive 3-D separation followed by reattachment and relaxation, resulting in strong distortion of the flow at the engine face (AIP). The correct prediction of the flow is a difficult challenge for statistical turbulence closures.

B. Computational Grids

The centerline of the duct was defined as the locus of the centers of gravity of $x = \text{const}$ sections. The computational domain is discretized using a multiblock grid, consisting of two structured blocks (Fig. 1). A block of rectangular cross section is used to discretize the centerline region of the duct, and an outer block discretizes the remaining part of the duct (Fig. 1). Communication between the two domains is ensured using a phantom-nodes technique [37]. Phantom nodes are not coincident with actual grid nodes and an interpolation algorithm is used to update phantom nodes from actual grid nodes at every subiteration.

C. Boundary Conditions

The inflow boundary-layer profile corresponds to the experimental data. The outflow static pressure applied as boundary condition at the outlet of the computational domain was adjusted separately for each turbulence closure to obtain the experimental wall pressure

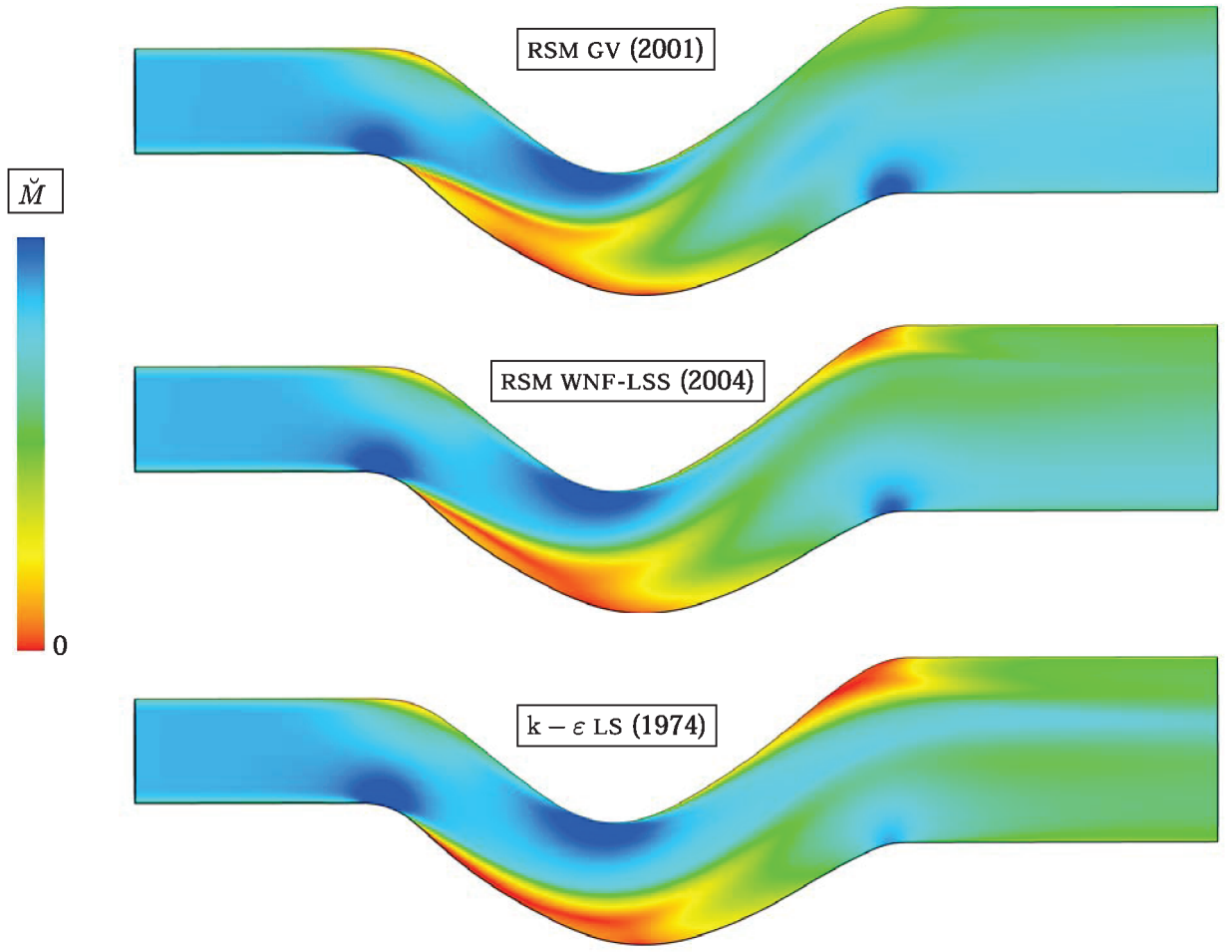

Fig. 3 Mach number contour plots at the symmetry plane computed using the GV [31] and the WNF– LSS [32] RSMs and the LS k-ε model [33] (2.9×10^6 points for grid_A).

distribution in the circumferential direction at plane 2 (Fig. 2) located near the entry of the channel, and as a consequence the same mass flow. Therefore, the predictions by the three turbulence models are compared at the same intake operating conditions.

D. Flowfield Structure at the Symmetry Plane

The flow structure is illustrated by the Mach number contours in the duct symmetry plane (Fig. 3) obtained from the numerical computations on grid_A (Table 2). All three models predict a large recirculation zone on the floor ($\phi_{EXP} = 180$ deg) of the duct, in the first S-bend, induced by the adverse pressure gradient, and flow acceleration at the ceiling ($\phi_{EXP} = 0$ deg) at the juncture between the two S-bends (Fig. 3). The GV [31] RSM predicts the largest separation region (Fig. 3) whereas the LS k-ε model [33] predicts the thinnest. More important, the GV [31] RSM predicts higher recirculation velocities (yellow and green levels) near the beginning of the S-bend (Fig. 3), associated with a higher blockage due to higher displacement thickness. As a result, the GV [31] RSM prediction of the flow relaxation (second S-bend and duct-exit) is fundamentally different from those obtained with the WNF–LSS [32] RSM and the LS k-ε model [33]. At the beginning of the straight part leading to the exit of the duct, at the ceiling in the symmetry plane ($\phi_{EXP} = 0$ deg), the GV [31] RSM does not predict separation, contrary to the two other models (WNF–LSS [32] RSM and LS [33] k-ε).

As a result, the predicted flow structure at the engine face (AIP), located near the beginning of the straight part of the duct exit, is very different between the three models (Fig. 3). The LS k-ε model [33] predicts a high-Mach-number region, which starts at the ceiling in the symmetry plane ($\phi_{EXP} = 0$ deg) at the middle of the duct where the two S-bends join, and continues, forming a jetlike structure, up to duct exit (blue level, Fig. 3). On the contrary, the GV [31] RSM does not predict such a jetlike structure at duct exit, nor does the WNF–LSS [32] RSM (Fig. 3), although the higher blockage predicted by the GV [31] RSM results in the absence of separation at the entry of the straight part of the duct exit, at the ceiling in the symmetry plane ($\phi_{EXP} = 0$ deg).

These initial results (Fig. 3) show that there are fundamental differences in predicted flow structure between the three models. Comparison with measurements of wall static pressures (Sec. III.F) and of total-pressure and Mach number profiles at the engine-face plane (Sec. III.G) will demonstrate that the correct (nearest to experimental) flow structure is that predicted by the GV [31] RSM.

E. Grid-Convergence Study

A grid-convergence study was performed using the GV [31] RSM. Previous grid-convergence studies [31,36] indicate that for complex flows with large separation, the GV [31] RSM correctly predicts larger separation and a more complex flow structure than the WNF–LSS [32] RSM or the LS k-ε model [33], and as a consequence, the grid converges slightly more slowly. Results were compared (Figs. 4–6) from computations on two different grids (Table 2), grid_A of 2.9×10^6 points and grid_B of 6.2×10^6 points, showing very good agreement, with the exception of the radial distribution of

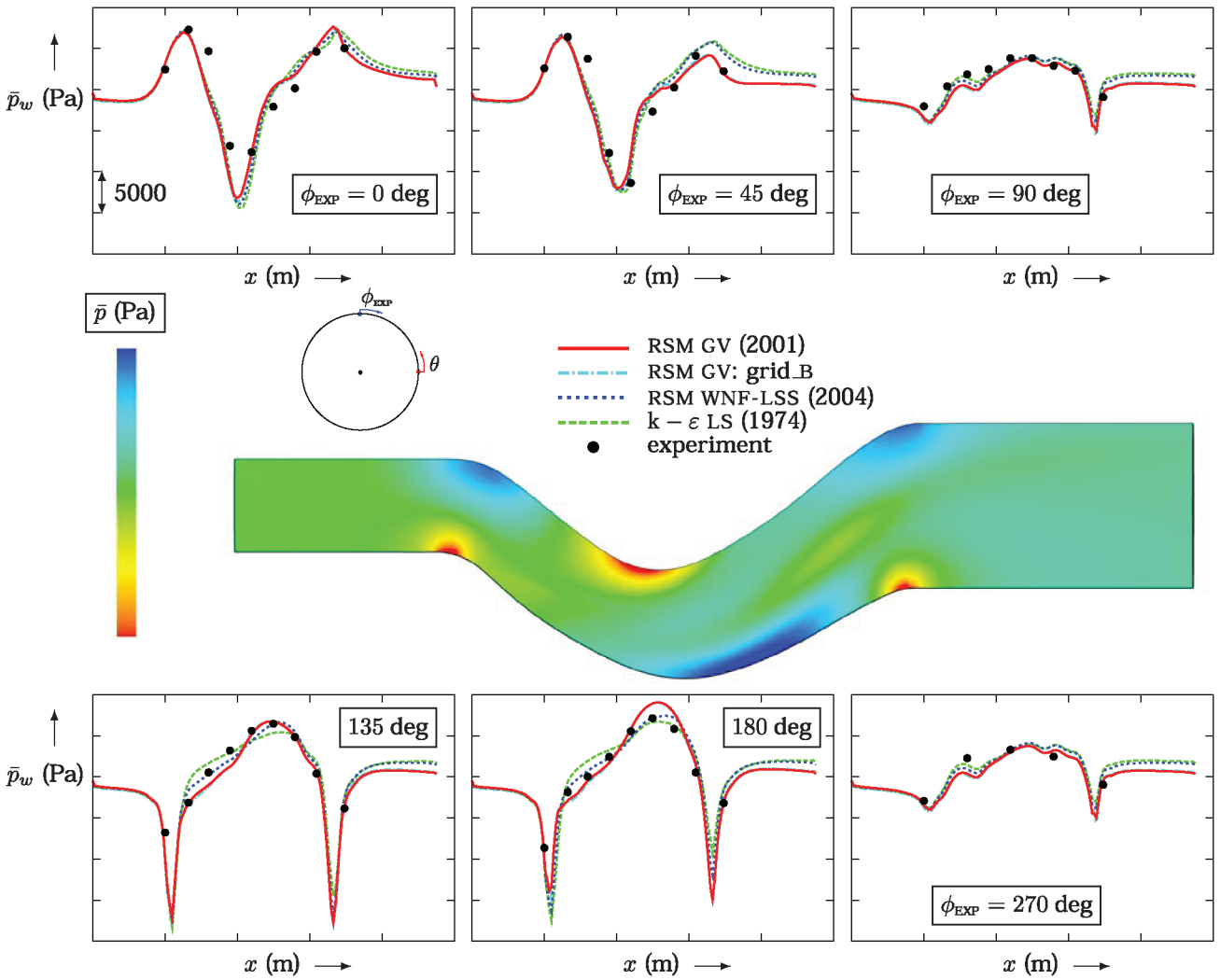

Fig. 4 Comparison of experimental wall-static-pressure $\bar{p}_w$ distributions in the streamwise direction x for different circumferential locations ϕ_{EXP}, with computations using the GV [31] and the WNF–LSS [32] RSMs and the LS k-ε model [33] (2.9×10^6 points for grid_A; static pressure $\bar{p}$ contours at the symmetry plane obtained from the GV [31] RSM calculations).

$\check{p}_t$ at the engine face for $\phi_{EXP} = 0$ deg (Fig. 6), where prediction is slightly improved by grid refinement. Therefore, computations were performed on the 2.9×10^6 points for the grid (grid_A, Table 2) using the GV [31] RSM, the WNF–LSS [32] RSM, and the LS k-ε model [33].

F. Wall-Static-Pressure Distributions

Wall-static-pressure distributions obtained from grid-converged computations (grid_A, Table 2) using the three turbulence models, were compared with measurements. Results are presented both as streamwise (x-wise) distributions at different angular locations ϕ_{EXP} (Fig. 4) and as circumferential distributions at different x planes (Fig. 5).

At plane 3, located just before the beginning of the first S-bend of the duct (Fig. 5), upstream influence is noticeable (Figs. 4 and 5) both on the floor (acceleration; $\phi_{EXP} = 0$ deg; Figs. 4 and 5,) and at the ceiling (deceleration; $\phi_{EXP} = 180$ deg; Figs. 4 and 5). In the first S-bend of the duct (planes 4, 5, and 6) the large separation observed on the floor ($\phi_{EXP} = 180$ deg) induces an inversion of high/low $\bar{p}_w$ regions between the ceiling (high level at planes 3 and 4 and a low level at plane 6; Fig. 5) and the floor (low level at planes 3 and 4, and high level at plane 6; Fig. 5) The inversion takes place somewhere near plane 5 (Fig. 5). In the second S-bend of the duct (planes 7, 8, and 9) an opposite inversion of high/low $\bar{p}_w$ regions between the ceiling ($\phi_{EXP} = 0$ deg; low level at planes 7, 8, and 9; Fig. 5) and the floor ($\phi_{EXP} = 180$ deg; high level at planes 7, 8, and 9; Fig. 5) is observed. The inversion takes place somewhere near plane 10 (Fig. 5).

The LS k-ε model [33] gives the worst predictions (Fig. 4), especially in the floor region ($\phi_{EXP} = 180, 135$ deg) of the first S-bend and at the outlet of the duct in the ceiling region ($\phi_{EXP} = 0, 45$ deg). These differences are more clearly seen in the circumferential plots at different measurement planes (Fig. 5). Recall that the exit-static-pressure boundary condition was adjusted separately for each turbulence model to obtain the experimental flow conditions at plane 2 (Fig. 2), where the wall static pressure $\bar{p}_w$ is nearly constant along the circumference of the duct (Fig. 2). The LS k-ε model [33] slightly overpredicts $\bar{p}_w$ at the lower part of the duct (140 deg $< \phi_{EXP} <$ 220 deg) at planes 4, 5, and 6 (Fig. 5). At the middle of the duct

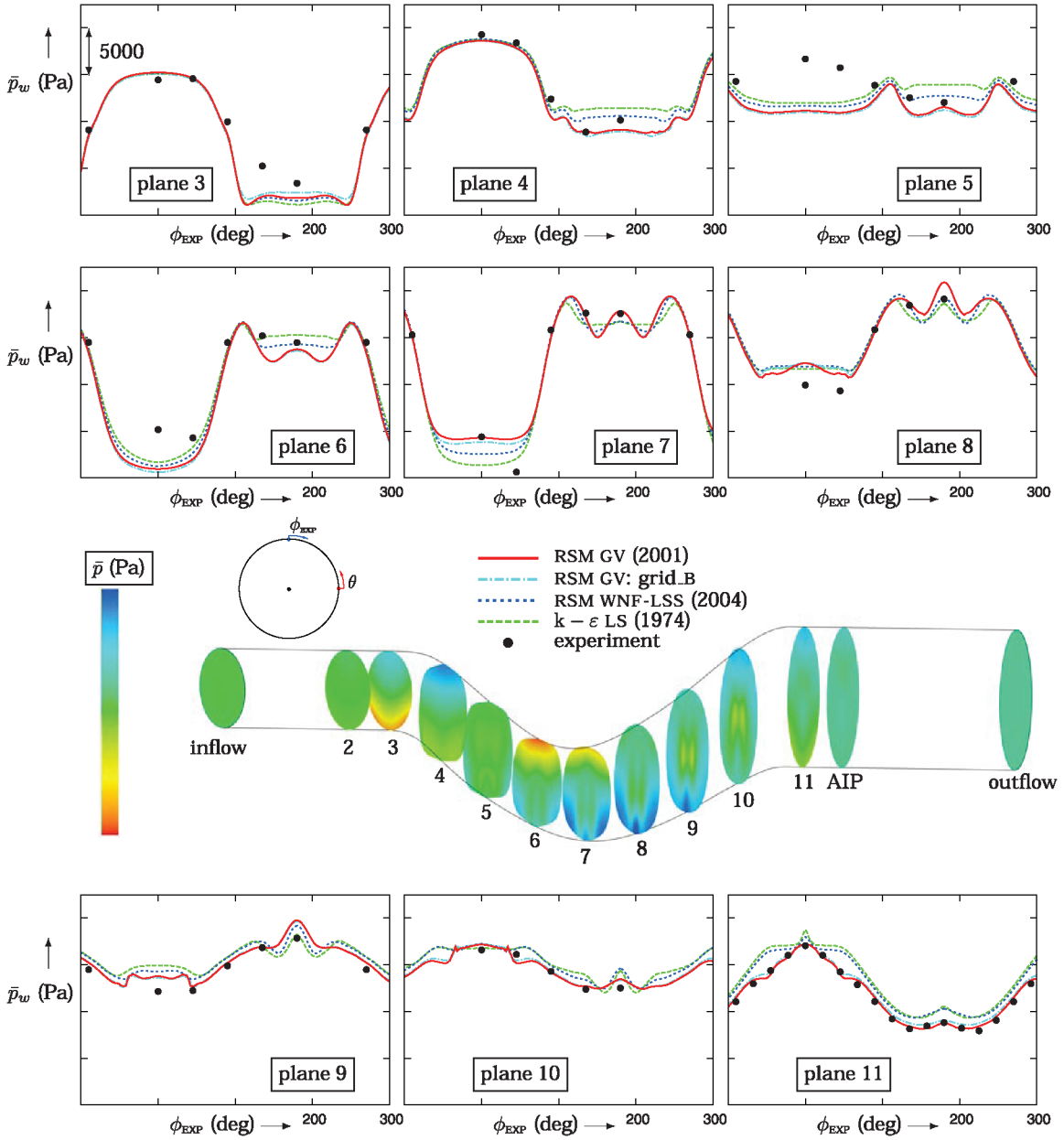

Fig. 5 Comparison of experimental wall-static-pressure $\bar{p}_w$ distributions in the circumferential direction ϕ_{EXP} for different streamwise stations (x = const planes), including the AIP, with computations using the GV [31] and the WNF–LSS [32] RSMs and the LS k-ε model [33] (2.9×10^6 points for grid_A; static pressure $\bar{p}$ contours at various x planes obtained from the GV [31] RSM calculations).

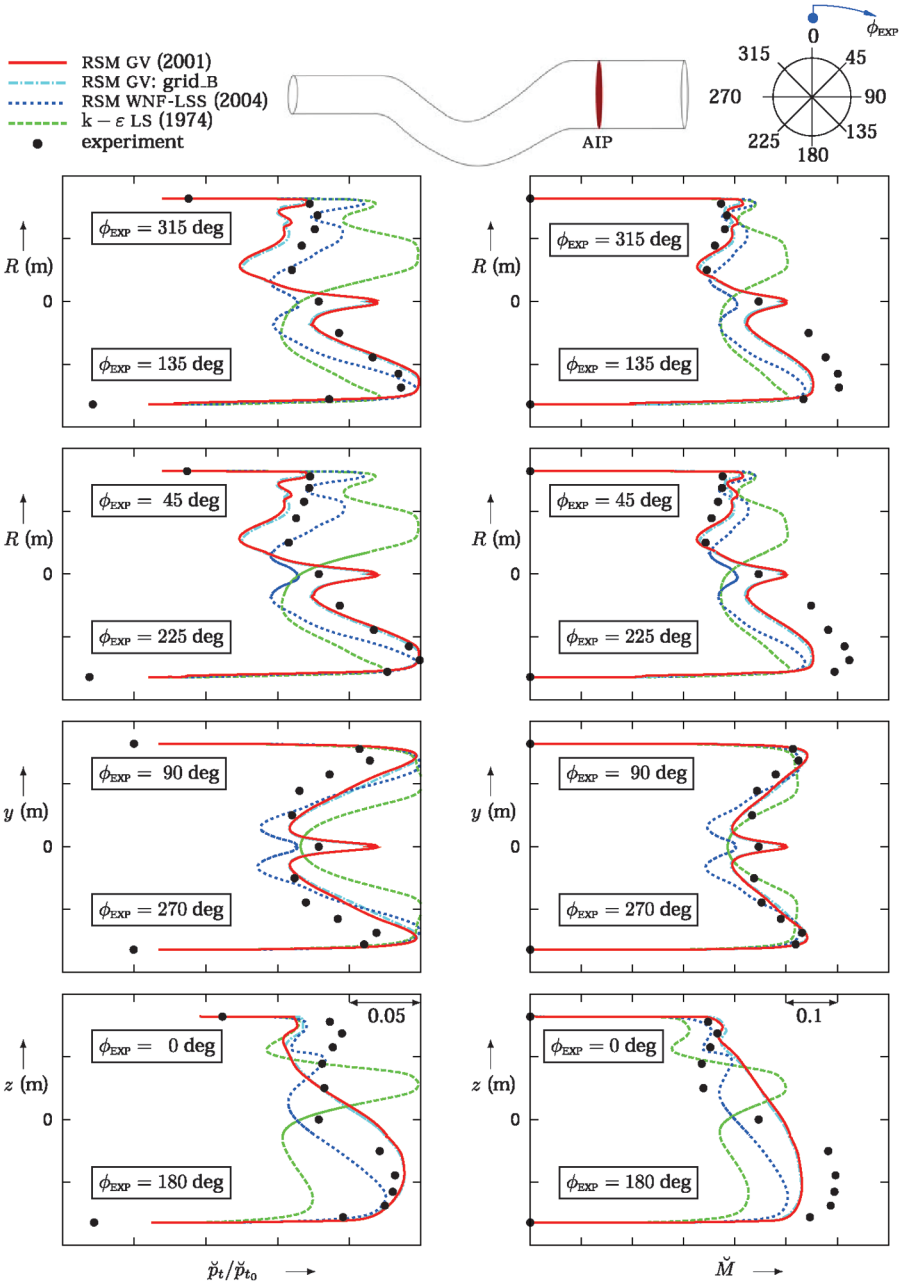

Fig. 6 Comparison of experimental total-pressure and Mach number radial distributions for different circumferential locations ϕ_{EXP} (eight rakes equispaced every 45 deg), at the AIP of circular cross section, with computations using the GV [31] and the WNF–LSS [32] RSMs and the LS k-ε model [33] (2.9×10^6 points for grid_A).

(plane 7; Fig. 5) the LS k-ε model [33] substantially underpredicts $\bar{p}_w$ at the upper part of the duct (-45 deg $< \phi_{EXP} < 45$ deg). At plane 11, just before the engine-face plane (AIP), the LS k-ε model [33] overpredicts $\bar{p}_w$.

The WNF–LSS [32] RSM predicts wall static pressures very similar both in shape and level to those given by LS k-ε model [33], except in the floor region ($\phi_{EXP} = 180$, 135 deg; Fig. 4) corresponding to the recirculation zone (planes 4, 5, and 6; Fig. 5) where the WNF–LSS [32] RSM improves upon the LS k-ε model [33].

The GV [31] RSM agrees overall quite well with measurements (Fig. 4). However, a slight underestimation of the wall static pressure $\bar{p}_w$ at the inlet of the channel in the ceiling region ($\phi_{EXP} = 0$, 45, 90 deg) is observed at the inversion plane 5 (Fig. 5), where the pressure-underprediction at the ceiling ($\phi_{EXP} = 0$ deg) is attributed to an underestimation of the detached flow that occurs on the floor ($\phi_{EXP} = 180$ deg). On the contrary, the wall static pressure is slightly overestimated on the floor ($\phi_{EXP} = 180$ deg) of the second S-bend of the duct (planes 8 and 9; Fig. 5). These discrepancies notwithstanding, the wall-static-pressure distributions predicted by the GV

Table 2 Computational grids[a]

	Grid_A	Grid_B
	O-grid (domain 1)	
$N_i(N_x)$	161	201
$N_j(N_\theta)$	161	201
$N_k(N_R)$	101	141
r_k	1.16	1.10
n_w^+	0.4	0.5
Grid points	2,618,021	5,696,541
	H-mesh (domain 2)	
$N_i(N_x)$	161	201
$N_j(N_y)$	41	49
$N_k(N_z)$	41	49
Grid points	270,641	482,601
Total grid points	2.89×10^6	6.18×10^6

[a]Where i, j, and k are grid directions; N_i, N_j, and N_k are the number of points; n_w^+ is the nondimensional distance of the first grid node away from the wall; r_k is the geometric progressional ratio; and x, R, and θ are local (at each x = const station) cylindrical coordinates with origin at the local section center of gravity.

[31] RSM at plane 11 (entry of the straight part of the duct exit; Fig. 5) are in excellent agreement with measurements.

Although the differences in $\bar{p}_w$ between the different models (Figs. 4, 5) are seemingly small (except for plane 11), they imply much larger difference in the flow structure and result in substantially different predictions of flow distortion at the AIP, which are revealed by detailed comparisons with rakes measurements obtained at the AIP (Sec. III.G).

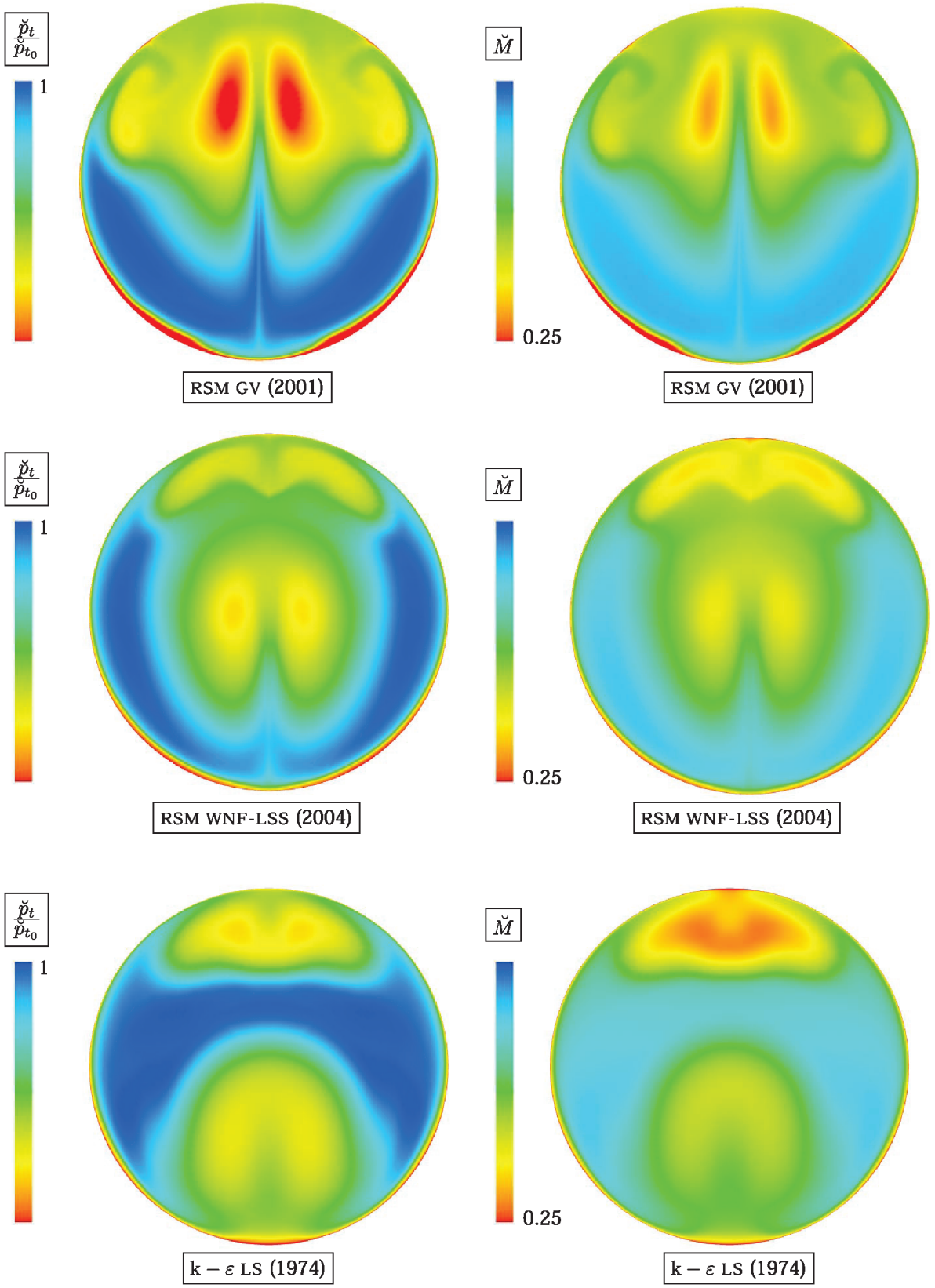

Fig. 7 Total-pressure and Mach number contour plots, at the AIP of circular cross section, computed using the GV [31] and the WNF–LSS [32] RSMs and the LS k-ε model [33] (same color range for all three models, 2.9 × 10^6 points for grid_A).

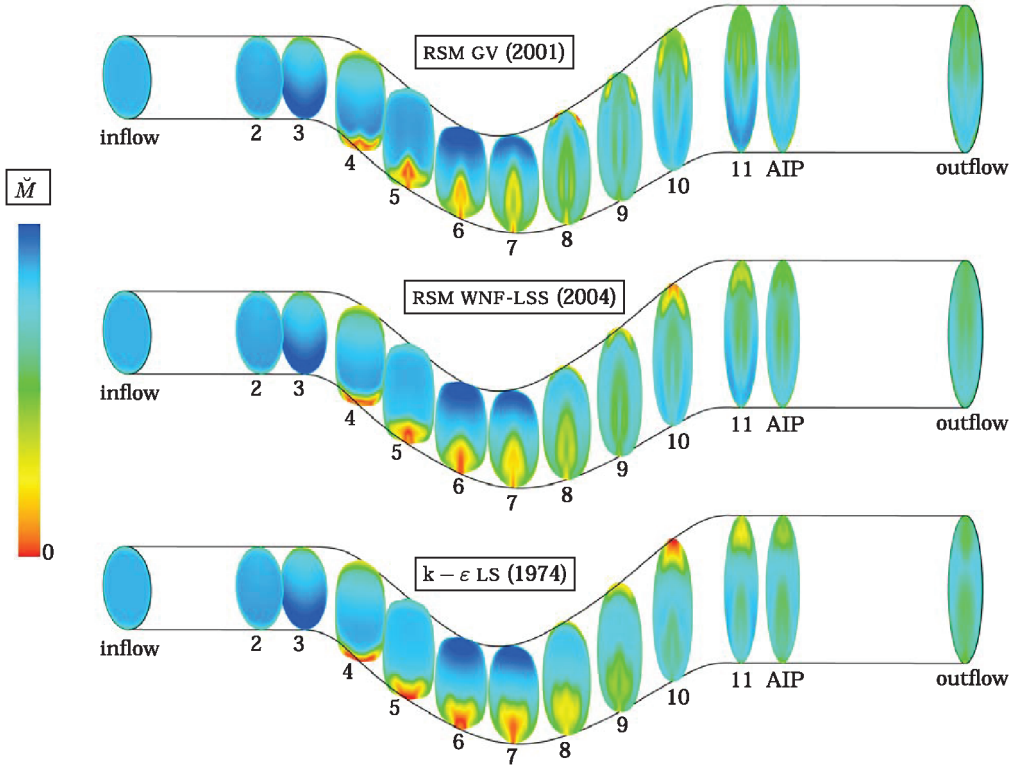

Fig. 8 Mach number contour plots for different streamwise stations ($x = \text{const}$ planes), including the AIP, computed using the GV [31] and the WNF–LSS [32] RSMs and the LS k-ε model [33] (2.9×10^6 points for grid_A).

G. Engine-Face Plane

Radial distributions of total pressure $\breve{p}_t$ and Mach number $\breve{M}$ at the AIP are compared with measurements (Fig. 6) that were available at eight circumferential positions $\phi_{\text{EXP}} = 0, 45, 90, 135, 180, 225, 270, 315$ deg. These comparisons (Fig. 6) reveal the important differences in predicted flow structure between the three models, which are further highlighted by contour plots of $\breve{p}_t$ and $\breve{M}$ at the engine-face plane (Fig. 7).

The LS k-ε model [33], as already mentioned when discussing the general flow structure (Sec. III.D; Fig. 3), predicts two lobes of high loss (low $\breve{p}_t$) separated by a region of clean flow (very low loss) at roughly three-fourths of the duct height (Fig. 7). Comparison with

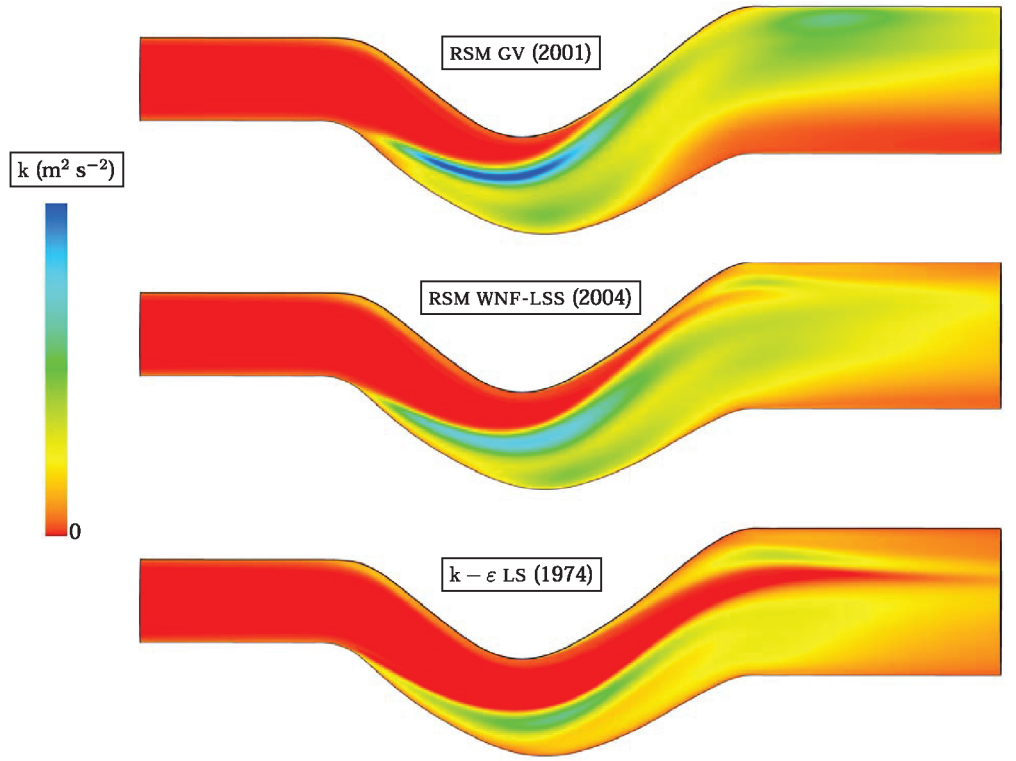

Fig. 9 Turbulent kinetic energy contour plots at the symmetry plane computed using the GV [31] and the WNF–LSS [32] RSMs and the LS k-ε model [33] (2.9×10^6 points for grid_A).

experimental data reveals (Fig. 6) that the flow structure predicted by the LS k-ε model [33] is wrong, since measured $\breve{p}_t$ at the symmetry plane ($\phi_{EXP} = 0$, 180 deg) of the duct at the AIP do not indicate a region of clean flow in the middle. This clean flow, erroneously predicted by the LS k-ε model [33], corresponds to the jetlike structure in the Mach number plots (Fig. 3), which is in complete disagreement with measurements ($\phi_{EXP} = 0, 45, 315$ deg; Fig. 6). As a conclusion, the flow structure predicted by the linear k-ε model [33] is entirely in error.

The GV [31] RSM predicts, at the AIP, two high-loss vortices (red levels in $\breve{p}_t$; Fig. 7), and two smaller secondary vortices (yellow level; Fig. 7). Comparison of the $\breve{p}_t$ distributions with measurements at the engine face (Fig. 6) shows that the GV [31] RSM gives the best agreement with measurements compared to the other two models. There are some discrepancies near the ceiling ($-45 \le \phi_{EXP} \le 45$), where the model somehow overpredicts $\breve{p}_t$ loss, but the overall structure is correct.

The spectacular improvement in flow-structure prediction, when comparing the GV [31] RSM and the LS k-ε model [33] computations with measurements (Fig. 6), is of course due to the fact that the seven-equation second-moment closure handles anisotropy [28] much better than the linear k-ε model [33]. The WNF–LSS [32] RSM also gives much better results than the linear k-ε model [33], but the agreement with measurements (Fig. 7) is less satisfactory compared to that obtained by the GV [31] RSM, everywhere except for $\breve{p}_t$ at $\phi_{EXP} = 45$ and 315 deg (Fig. 7).

Concerning the discrepancies between experiments and computations observed (Fig. 6) near the ceiling (-45 deg $\le \phi_{EXP} \le +45$ deg) it should be noted that the experimental flow is not symmetric around the symmetry plane ($y = 0$). This can be seen by comparing the $\breve{p}_t$ measurements at $\phi_{EXP} = 45$ and 315 deg (Fig. 6). These two rakes are symmetric on each side of the $\phi_{EXP} = 0$ deg symmetry plane, but measurements exhibit asymmetry. The origin of this problem can be traced to an observed asymmetry of the flow at the entry of the measurement section. Furthermore, contrary to wall pressure taps, measurements at the AIP are particularly intrusive, the total-pressure probes being mounted on eight struts held on a centerbody located at roughly $1/6\, D_{AIP}$ downstream of the AIP (D_{AIP} is the diameter of the circular cross section of the AIP). The obstruction induced by the centerbody struts–rakes arrangement influences the shape of the streamlines upstream of the AIP. Although losses are mainly produced upstream of the AIP, the upstream influence of the centerbody struts–rakes obstacle modifies the measured flow at the AIP. This can partly explain the observed discrepancies at the AIP (Fig. 6) between the GV [31] RSM prediction and experimental data, which is in very good agreement further upstream (Fig. 5, plane 11).

H. Detailed Flow Analysis

The comparisons with available measurements (Figs. 4–6) suggest that the GV [31] RSM gives the best prediction of the flow (Fig. 7). It is useful to keep in mind that the seven-equation WNF–LSS [32] RSM also improves upon the k-ε model [33], but less so than the GV [31] RSM. Examination of Mach number contour plots at various planes (Fig. 8) shows that the separated flow structure at the descending first S-bend on the duct floor, predicted by the LS k-ε model [33] is very different from that predicted by the GV [31] RSM, already at plane 4.

The decelerated flow region predicted by the k-ε model [33] (planes 5, 6, 7, and 8) does not extend beyond duct half-height (Fig. 8), whereas it nearly reaches the duct ceiling in the GV [31] RSM prediction at plane 8 (Fig. 8). As a consequence, the LS k-ε model [33] erroneously predicts a large separation at duct ceiling at plane 10 (Fig. 8).

Analogous conclusions are obtained from the contour plots of turbulence kinetic energy $k = \frac{1}{2}\widetilde{u_i'' u_i''}$ (Figs. 9 and 10). The region of high turbulence predicted by the LS k-ε model [33] is confined below duct centerline (plane 8; Fig. 10) whereas it extends up to $\frac{3}{4}$ of duct height in the GV [31] RSM predictions (plane 8, Fig. 10). Interestingly, in the relaxation region (planes 9, 10, 11, AIP; Fig. 10) the high-turbulence region predicted by the GV [31] RSM migrates from floor to ceiling, whereas the k-ε model [33] erroneously predicts two separate high-turbulence regions: one that remains confined near the

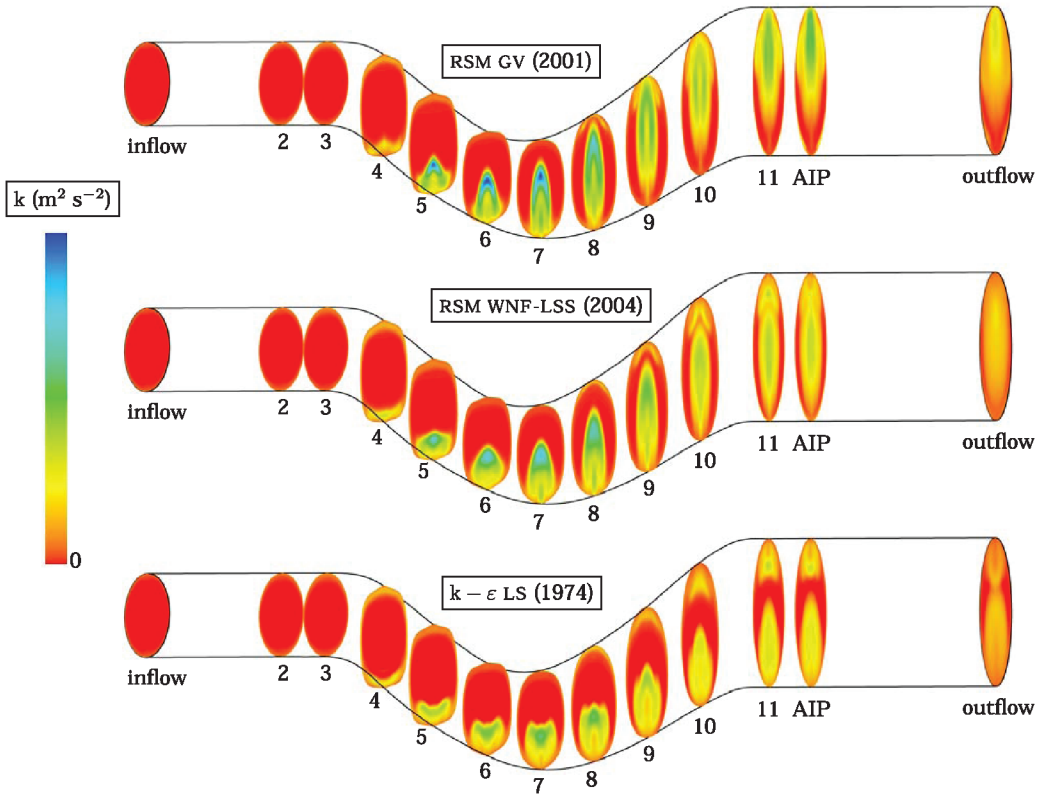

Fig. 10 Turbulent kinetic energy contour plots for different streamwise stations (x = const planes), including the AIP, computed using the GV [31] and the WNF–LSS [32] RSMs and the LS k-ε model [33] (2.9×10^6 points for grid_A).

floor and a second one that is generated near the ceiling after the erroneously predicted separation at planes 9 and 10 (Figs. 9 and 10).

It is plausible that the high turbulence-levels predicted by the GV [31] RSM up to the duct ceiling (planes 8 and 9; Fig. 10) are responsible of the fact that the flow remains attached at the ceiling. The predictions of the WNF–LSS [32] RSM reveal both the definite advantage of using seven-equation anisotropy-resolving second-moment closures [28], in that high turbulence is predicted beyond duct centerline (Figs. 9 and 10) thus partially limiting separation at plane 10 (Fig. 8), but also the major impact of the coefficient function C_{ϕ}^{RH} (Table 1) on the results.

Since the GV [31] RSM gives the best prediction of both wall pressure distributions (Figs. 4 and 5) and of the flow structure at the AIP (Fig. 6), the results obtained with this model were used to generate flow streamlines (Fig. 11). Examination (Fig. 11) of streamwise vorticity $\breve{\omega}_s \breve{V} := \boldsymbol{\omega}.\mathbf{V}$ at plane 3 (just at the beginning of the descent of the first S-bend), at plane 8 (just at the beginning of the ascending part of the second S-bend) and at the AIP, indicates the presence at the AIP of four vortical structures, two counter-rotating pairs on each side of the $y = 0$ xz symmetry plane. Regions of $\breve{\omega}_s \breve{V}$ colored in blue correspond to vortical structures rotating clockwise around the flow direction for an observer looking downstream (streamwise vorticity $\breve{\omega}_s$ positive) while regions colored in red rotate in the opposite sense. The traces of these vortical structures at the AIP roughly correspond to the regions of high loss observed in the $\breve{p}_t$ distribution (Fig. 7). The correspondence is not exact, in that the locus of highest loss does not exactly correspond with the region of highest $\breve{\omega}_s \breve{V}$ (Fig. 11).

The largest vortical structure ($\breve{\omega}_s > 0$) at the $y < 0$ part of the AIP (on the right of the $y = 0$ symmetry plane looking downstream) is generated by the large 3-D flow separation occurring downstream of plane 3 on the descending part of the first S-bend (lower-separation vortex; Fig. 11). Streamlines initiating in the boundary layer of plane 3 (-180 deg $\lessapprox \phi_{\mathrm{EXP}} \lessapprox -45$ deg) flow clockwise towards the $y = 0$ symmetry plane ($\phi_{\mathrm{EXP}} = -180$ deg), over the concave inner surface of the duct, and form a tornadolike structure (Fig. 11). This tornadolike structure is deflected by the $y = 0$ symmetry plane, and lifts off from the lower wall forming a large vortical structure moving downstream (Fig. 11). At plane 8, this vortical structure corresponds to the high-loss region (Fig. 11) and, moving downstream, approaches the upper wall at the AIP.

Streamlines initiating in the boundary layer of plane 3 in the region (-45 deg $\lessapprox \phi_{\mathrm{EXP}} \lessapprox 0$ deg) move only very slightly clockwise in the descending part of the first S-bend. At the ascending part of the second S-bend, streamwise vorticity in the boundary layer changes sign, and the upper-wall boundary-layer streamlines move anti-clockwise (plane 8; Fig. 11), and under the influence of the strong adverse pressure-gradient observed in the wall pressure distribution

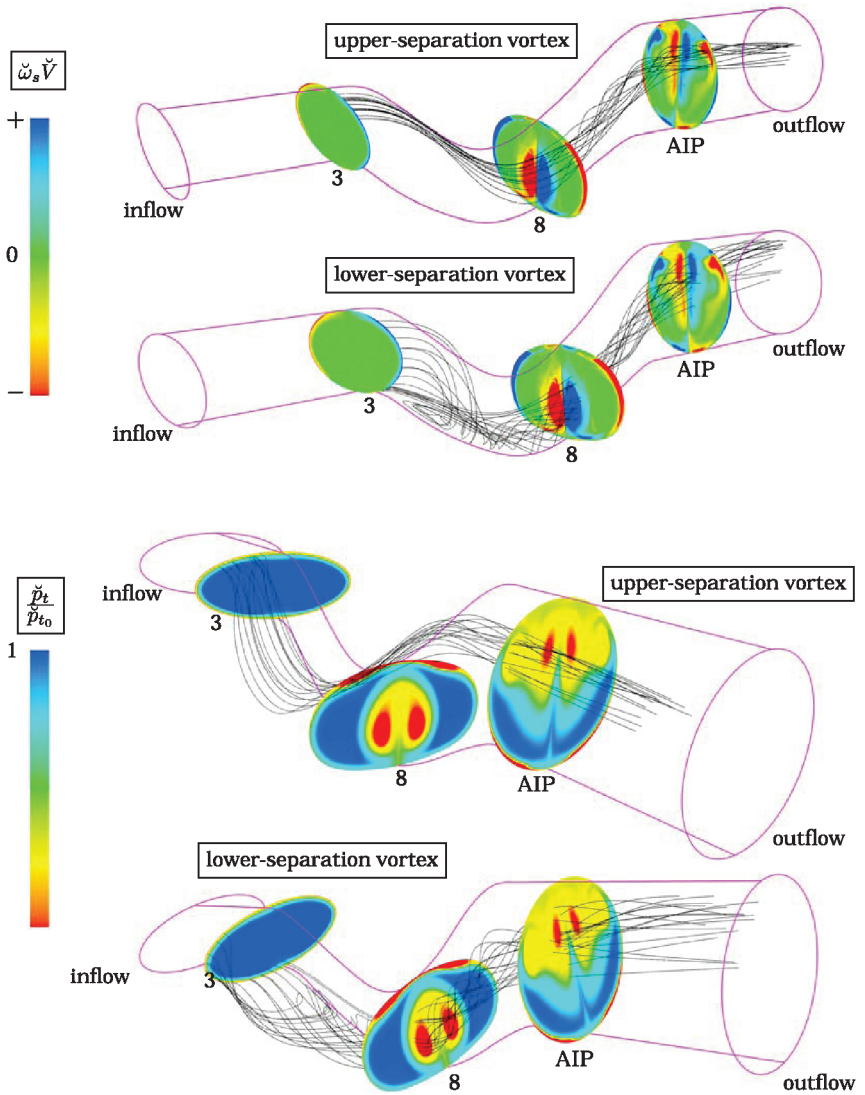

Fig. 11 Selected streamlines of the flow computed using the GV [31] RSM (2.9×10^6 points for grid A; Table 2), illustrating the two vortices that dominate the flow to the right of the symmetry plane $y = 0$ (two corresponding counter-rotating vortices exist on the left of the symmetry plane $y = 0$), induced by 3-D separation on the lower and upper parts of the duct wall (front view with color plots of streamwise vorticity $\breve{\omega}_s \breve{V} := \breve{\omega} \cdot \tilde{\mathbf{V}} = \mathrm{rot}\tilde{\mathbf{V}} \cdot \tilde{\mathbf{V}}$, and rear view with color plots of total pressure $\breve{p}_t$).

for $\phi_{\mathrm{EXP}} = \pm 45$ deg (Fig. 4), they roll up to form an upper-wall separation vortex rotating anticlockwise (Fig. 11). The upper-separation vortices (Fig. 11) are discernible in the $\breve{p}_t$ plots obtained with the GV [31] RSM at the AIP $\phi_{\mathrm{EXP}} = 45$ and 315 deg (Fig. 6) and were referred to as secondary vortices in Sec. III.G. Note (Fig. 6) that the GV [31] RSM is the only model that correctly predicts the distributions of $\breve{p}_t$ and $\breve{M}$ at $\phi_{\mathrm{EXP}} = 45$ and 315 deg at the AIP and that also correctly predicts a clean-flow region at $\phi_{\mathrm{EXP}} = 180$ deg at the AIP.

The satisfactory prediction of both types of vortical structures (Fig. 11), and of the blockage they induce on the flow (and on one another) is essential for correct prediction of this complex flow. The linear k-ε model [33] completely fails in correctly predicting the liftoff of the lower-wall separation, which remains confined near the floor at the AIP (Fig. 7). As a result, the blockage of the flow at the ceiling induced by the lower-separation vortex is severely underestimated. Therefore, the linear k-ε model [33] overpredicts flow separation at the ceiling (plane 10, Fig. 8). At the AIP, the linear k-ε model [33] erroneously predicts the lower-separation vortices very near the lower wall and the upper-separation vortices very near $\phi_{\mathrm{EXP}} = 0$ deg. The WNF–LSS [32] RSM substantially improves upon the linear k-ε model [33], predicting a liftoff of the lower-separation vortices at the AIP (Fig. 7), but not sufficiently to push sideways the two upper-separation vortices.

IV. Conclusions

In the present work, predictions using two wall-topology-free second-moment closures, the GV [31] RSM and the WNF–LSS [32] RSM, were compared with measurements and with predictions using the baseline LS k-ε model [33] for a realistic aircraft-engine intake 2S-duct. The results indicate that the GV [31] RSM predicts with reasonable accuracy this difficult test case, for which the baseline k-ε model [33] completely fails. This result confirms previous investigations on strongly diffusing S-duct flows. The superior results obtained by the GV [31] RSM compared to the WNF–LSS [32] RSM further highlight the importance of the modeling of the rapid-redistribution terms (this is the main difference between the two RSMs) in the Reynolds-stress closure in correctly predicting separated flows. Detailed analysis of the flowfield using the closest to measurement prediction (the GV [31] RSM) indicates that flow distortion at the AIP is dominated by the interaction of two pairs of counter-rotating vortical structures, corresponding to lower separation in the first S-bend and upper separation in the second S-bend. The lower-separation vortices lift off from the floor of the duct and influence the formation of the upper-separation vortices. Before reaching the AIP, the two systems of vortices interact strongly.

Acknowledgments

The present work was conducted within the Direction Générale de l'Armement (DGA)-funded research project CACV (Conception Aérodynamique et Contrôle du Vol des Avions de Combat). Computations were performed using high-performance-computing resources from Grand Equipement National de Calcul Intensif, Institut pour le Développement de Ressources en Informatique Scientifique (GENCI-IDRIS, grants 2008-000218 and 2009-000218). The authors are listed alphabetically.

References

[1] Shirkey, M. D., "The Results of Low-Speed Wind Tunnel Tests to Investigate the Effects of the NASA Refan JT8D Engine Nacelles on the Stability and Control Characteristics of the Boeing 727–200," NASA Lewis Research Center, CR-1973-134503, Cleveland, OH, Nov. 1973.

[2] Steenken, W. G., Williams, J. G., and Walsh, K. R., "Inlet Flow Characteristics During Rapid Maneuvers for an F/A-18A Airplane," NASA Dryden Flight Research Center, TM-206587, Edwards AFB, CA, Oct. 1999.

[3] Burcham, F. W., Jr., Ray, R. R., Conners, T. R., and Walsh, K. R., "Propulsion Flight Research at NASA Dryden from 1967 to 1997," NASA Dryden Flight Research Center, TP-206554, Edwards AFB, CA, July 1998; also AIAA Paper 1998-3712, Cleveland, OH, July 1998.

[4] Newcome, L. R., *Unmanned Aviation*, AIAA, Reston, VA, 2004.

[5] Cummings, R. M., Morton, S. A., and Siegel, S. G., "Numerical Prediction and Wind Tunnel Experiment for a Pitching Unmanned Combat Air Vehicle," *Aerospace Science and Technology*, Vol. 12, 2008, pp. 355–364. doi:10.1016/j.ast.2007.08.007

[6] Tormalm, M., "Design and Analysis of Compact UAV Ducts," AIAA Applied Aerodynamics Conf., AIAA Paper 2006-2828, San Francisco, 5–8 June 2006.

[7] Johansson, M., "Propulsion Integration in a UAV," AIAA Applied Aerodynamics Conf., AIAA Paper 2006-2834, San Francisco, June 2006.

[8] Kirk, A. M., Gargoloff, J. I., Rediniotis, O. K., and Cizmas, P. G. A., "Numerical and Experimental Investigation of a Serpentine Inlet Duct," *International Journal of Computational Fluid Dynamics*, Vol. 23, No. 3, March 2009, pp. 245–258. doi:10.1080/10618560902835558

[9] Brear, M. J., Warfield, Z., Magnus, J. F., Bradomm, S., Paduano, J. D., and Philhower, J. S., "Flow Separation Within the Engine Inlet of an Uninhabited Combat Air Vehicle (UCAV)," *Journal of Fluids Engineering*, Vol. 126, March 2004, pp. 266–272. doi:10.1115/1.1667885

[10] Foster, J., Wendt, B. J., Reichert, B. A., and Okiishi, T. H., "Flow Through a Rectangular-to-Semiannular Diffusing Transition Duct," *Journal of Propulsion and Power*, Vol. 13, No. 2, March 1997, pp. 312–317. doi:10.2514/2.5165

[11] Berrier, B. L., and Allan, B. G., "Experimental and Computational Evaluation of Flush-Mounted, S-Duct Inlet," AIAA Paper 2004-0764, 2004.

[12] Seddon, J., and Goldsmith, E. L., *Intake Aerodynamics*, 2nd ed., AIAA, Reston, VA, 1999, pp. 266–289, chap. 11.

[13] Williams, D. D., and Surber, L. E., "Intake/Engine Compatibility," *Practical Intake Aerodynamic Design*, edited by J. Seddon and E. L. Goldsmith, AIAA, Reston, VA, 1993, pp. 21–71, chap. 2.

[14] Cumpsty, N. A., *Compressor Aerodynamics*, Addison Wesley Longman, Essex, England, U.K., 1989, pp. 359–409, chap. 9.

[15] Harloff, G. J., Smith, C. F., Bruns, J. E., and DeBonis, J. R., "Navier–Stokes Analysis of Three-Dimensional S-Ducts," *Journal of Aircraft*, Vol. 30, No. 4, July 1993, pp. 526–533. doi:10.2514/3.46375

[16] Wellborn, S. R., Reichert, B. A., and Okiishi, T. H., "Study of the Compressible Flow in a Diffusing S-Duct," *Journal of Propulsion and Power*, Vol. 10, No. 5, Sept. 1994, pp. 668–675. doi:10.2514/3.23778

[17] Gopaliya, M. K., Kumar, M., Kumar, S., and Gopaliya, S. M., "Analysis of Performance Characteristics of S-Shaped Diffuser with Offset," *Aerospace Science and Technology*, Vol. 11, 2007, pp. 130–135. doi:10.1016/j.ast.2006.11.003

[18] Wilcox, D. C., *Turbulence Modelling for CFD*, 2nd ed., DCW Industries, La Cañada, CA, 1998.

[19] Rabe, A. C., "Effectiveness of a Serpentine Inlet Duct Flow Control System at Design and Off-Design Simulated Flight Conditions," Ph.D., Thesis, Virginia Polytechnic Inst. and State Univ., Blacksburg, VA, Aug. 2003.

[20] Nichols, R. H., "Calculation of the Flow in a Circular S-Duct Inlet," AIAA Aerospace Science Meeting, AIAA Paper 1991-0174, Reno, NV, Jan. 1991.

[21] Tsai, H. M., Guarino, L., and Lee, K. M., "Numerical Prediction of 3-D S-Ducts using the Johnson-King Model," AIAA Aerospace Science Meeting, AIAA Paper 1995-0359, Reno, NV, Jan. 1995.

[22] Anderson, B. H., Reddy, D. R., and Kapoor, K., "Study on Computing Separating Flows within a Diffusing Inlet S-Duct," *Journal of Propulsion and Power*, Vol. 10, No. 5, Sept. 1994, pp. 661–667. doi:10.2514/3.23777

[23] Zhang, W. L. D., Knight, D., and Smith, D., "Automated Design of a Three-Dimensional Subsonic Diffuser," *Journal of Propulsion and Power*, Vol. 16, No. 6, Nov.–Dec. 2000, pp. 1132–1140. doi:10.2514/2.5688

[24] Menzies, R. D. D., Badcock, K. J., Barakos, G. N., and Richards, B. E., "Validation of the Simulation of Flow in an S-Duct," AIAA Applied Aerodynamics Meeting, AIAA Paper 2002-2808, St. Louis, MO, June 2002.

[25] Yaras, M. I., and Grosvenor, A. D., "Evaluation of 1- and 2-Equation Low-*Re* Turbulence Models, Part II—Vortex-Generator Jet and Diffusing S-Duct Flows," *International Journal for Numerical Methods*

in Fluids, Vol. 42, 2003, pp. 1293–1319.
doi:10.1002/fld.585

[26] Saha, K., Singh, S. N., Seshadri, V., and Mukhopadhyay, S., "Computational Analysis on Flow Through Transition S-Diffusers: Effect of Inlet Shape," *Journal of Aircraft*, Vol. 44, No. 1, Jan. 2007, pp. 187–193.
doi:10.2514/1.22828

[27] Vallet, I., "Reynolds-Stress Modelling of 3-D Secondary Flows with Emphasis on Turbulent Diffusion Closure," *Journal of Applied Mechanics*, Vol. 74, No. 6, Nov. 2007, pp. 1142–1156.
doi:10.1115/1.2722780

[28] Leschziner, M. A., "Turbulence Modelling for Separating Flows with Anisotropy-Resolving Closures," *Philosophical Transactions of the Royal Society of London, Series A: Mathematical and Physical Sciences*, Vol. 358, 2000, pp. 3247–3277.
doi:10.1098/rsta.2000.0707

[29] Hanjalić, K., "Will RANS Survive LES? A View of Perspectives," *Journal of Fluids Engineering*, Vol. 127, Sept. 2005, pp. 831–839.
doi:10.1115/1.2037084

[30] Gerolymos, G. A., and Vallet, I., "Near-Wall Reynolds-Stress 3-D Transonic Flows Computation," *AIAA Journal*, Vol. 35, No. 2, Feb. 1997, pp. 228–236.
doi:10.2514/2.110

[31] Gerolymos, G. A., and Vallet, I., "Wall-Normal-Free Near-Wall Reynolds-Stress Closure for 3-D Compressible Separated Flows," *AIAA Journal*, Vol. 39, No. 10, Oct. 2001, pp. 1833–1842.
doi:10.2514/2.1179

[32] Gerolymos, G. A., Sauret, E., and Vallet, I., "Contribution to the Single-Point-Closure Reynolds-Stress Modelling of Inhomogeneous Flow," *Theoretical and Computational Fluid Dynamics*, Vol. 17, Nos. 5–6, Sept. 2004, pp. 407–431.
doi:10.1007/s00162-004-0109-5

[33] Launder, B. E., and Sharma, B. I., "Application of the Energy Dissipation Model of Turbulence to the Calculation of Flows near a Spinning Disk," *Letters in Heat and Mass Transfer*, Vol. 1, 1974, pp. 131–138.
doi:10.1016/0094-4548(74)90150-7

[34] Lumley, J. L., "Computational Modeling of Turbulent Flows," *Advances in Applied Mechanics*, Vol. 18, 1979, pp. 123–176.
doi:10.1016/S0065-2156(08)70266-7

[35] Launder, B. E., and Shima, N., "2-Moment Closure for the Near-Wall Sublayer: Development and Application," *AIAA Journal*, Vol. 27, No. 10, Oct. 1989, pp. 1319–1325.
doi:10.2514/3.10267

[36] Gerolymos, G. A., Sauret, E., and Vallet, I., "Oblique-Shock-Wave/Boundary-Layer Interaction Using Near-Wall Reynolds-Stress Models," *AIAA Journal*, Vol. 42, No. 6, June 2004, pp. 1089–1100.
doi:10.2514/1.1984

[37] Gerolymos, G. A., and Vallet, I., "Mean-Flow-Multigrid for Implicit Reynolds-Stress-Model Computations," *AIAA Journal*, Vol. 43, No. 9, Sept. 2005, pp. 1887–1898.
doi:10.2514/1.13847

[38] Gerolymos, G. A., and Vallet, I., "Implicit Mean-Flow-Multigrid Algorithms for Reynolds-Stress-Model Computations of 3-D Anisotropy-Driven and Compressible Flows," *International Journal for Numerical Methods in Fluids*, Vol. 61, No. 2, Sept. 2009, pp. 185–219.
doi:10.1002/fld.1945